Rough Surfaces: is the dark stuff just shadow?

"Who knows what evil lurks in the hearts of men? The Shadow knows!" [1]

Jeffrey N. Cuzzi[1], Lindsey B. Chambers[2], Amanda R. Hendrix[3]

[1]Ames Research Center, NASA; [2]University of California, Santa Cruz; [3]PSI, inc.

Abstract

Remote observations of the surfaces of airless planetary objects are fundamental to inferring the physical structure and compositional makeup of the surface material. A number of forward models have been developed to reproduce the photometric behavior of these surfaces, based on specific, assumed structural properties such as macroscopic roughness and associated shadowing. Most work of this type is applied to geometric albedos, which are affected by complicated effects near zero phase angle that represent only a tiny fraction of the net energy reflected by the object. Other applications include parameter fits to resolved portions of some planetary surface as viewed over a range of geometries. The spherical albedo of the entire object (when it can be determined) captures the net energy balance of the particle more robustly than the geometric albedo. In most treatments involving spherical albedos, spherical albedos and particle phase functions are often treated as if they are independent, neglecting the effects of roughness. In this paper we take a different approach. We note that whatever function captures the phase angle dependence of the brightness of a realistic *rough, shadowed, flat* surface element relative to that of a smooth granular surface of the same material, it is manifested directly in both the integral phase function *and* the spherical albedo of the object. We suggest that, where broad phase angle coverage is possible, spherical albedos may be easily corrected for the effects of shadowing using *observed* (or assumed) phase functions, and then modeled more robustly using smooth-surface regolith radiative transfer models *without* further imposed (forward-modeled) shadowing corrections. Our approach attributes observed "powerlaw" phase functions of various slope (and "linear" ranges of magnitude-*vs.*-phase angle) to shadowing, as have others, and goes in to suggest that regolith-model-based inferences of composition based on shadow-uncorrected spherical albedos overestimate the amount of absorbing material contained in the regolith.

---

[1]From the 1930s radio serial "The Shadow", originated by Street and Smith Publications, inc. (Stedman 1977)

1 Introduction

Inference of surface composition from remote sensing is a core tool in planetary science. In studies of planetary rings, there is added motivation to obtain quantitative results for compositional fractions because the relative abundances of icy and nonicy material can be diagnostic of meteoroid bombardment and ring age. Classical treatments (Harris 1961) show how the phase function of an object plays a key role in relating its observed brightness at some arbitrary phase angle (generally called I/F, as discussed below) *back* to either its geometric or "spherical" albedo, either of which can constrain composition (see next section for definitions). If the phase function is not measured (generally the case for remote objects not visited by spacecraft), then representative phase functions (for, *e.g..*, inner and outer solar system, dark and bright, objects) can serve as substitutes, with some uncertainty. Most compositional modeling of this kind has been applied to low phase angle observations where surface shadowing plays a small role (see section 1.5) and low reflectivity is primarily due to absorbing materials mixed into the near-surface regolith (eg. Emery and Brown 2004, Cruikshank *et al.* 2005). These observations are transformed into geometric albedos, the reflectivity at zero phase angle, and model inferences are often not even corrected for shadowing.

The need to incorporate roughness in compositional modeling is certainly not unknown to aficionados of the technique. Detailed algorithms for calculating these effects have been known for decades (Lumme and Bowell 1981a,b, Hapke 1993, his chapter 12). The former calculate the shadowing for single scattering separately in porous surfaces and macroscopic "holes", adding in a model for multiple scattering in both structures. The latter assume a faceted surface structure and calculate a shadowing correction which is applied to an independently modeled smooth-surface albedo, and neglect multiple scattering. Both are *forward models*, based on assumed parameters. For a broad discussion and background of planetary surface photometry and the effects of roughness and shadowing, the reader is also referred to Shkuratov *et al.* (2005, 2012), Hapke (2013) and Shkuratov *et al.* (2013), as well as Mushkin and Gillespie (2006), Jehl *et al.* (2008), Muinonen *et al.* (2011), and Goguen *et al.* (2010) which cover a representative selection of approaches and targets. In a few recent studies, extensive grid-based, Bayesian, or genetic algorithms have been used to separate roughness and compositional effects (Cord *et al.* 2003, 2005, Souchon *et al.* 2011, Pilorget *et al.* 2016, Domingue *et al.* 2016).

In the planetary rings literature, attention to the effects of shadowing on particle albedo has been mixed. Shadowing was untreated in spherical albedo modeling by Doyle *et al.* (1989), Cuzzi and Estrada (1998), Bradley *et al.* (2010, 2013), Elliott and Esposito (2011), and Poulet and Cuzzi (2002). Poulet *et al.* (2003) worked with the *near*-zero phase angle reflectivity of a ring particle, after removing optical depth and geometry effects, and also neglected roughness treatments; they needed to add some 5-10% carbon to the ring material to match the overall albedo. Poulet *et al.* (2002), also working over a small range of low phase angles, explicitly treated ring particle roughness using both the Hapke (1993) and Shkuratov *et al.* (1999) models, finding the A and B ring particles to be rougher, but did not go so far as to derive particle compositions.

Ciarniello *et al.* (2011) and Filacchione *et al.* (2013) normalize spectra of icy moons in an attempt to remove the effect of roughness, and make use of the secondary effect of internal absorbing material on depth of ice absorption bands (ring spectra were not quantitatively analyzed for composition), and Hedman *et al.* (2013) also work with moderate phase angle reflectivities but do not account for surface roughness. It is possible, but has not been demonstrated, that modeling spectral band shape and contrast alone, as in Ciarniello *et al.* (2011), Clark *et al.* (2012), Filacchione *et al.* (2013), and Hedman *et al.* (2013) can eliminate the effects of surface roughness, but given the number of parameters available to absorb the effects, including continuum absorber and regolith grain properties,

one remains concerned (see end of section 2). For example, Hedman *et al.* (2013) analyzed moderate phase angle brightness values using a Shkuratov model for a smooth, flat surface, inferring significant radial variations in "effective" grain size that are strongly correlated with local optical depth variations across the rings. However, both on-surface shadowing and interparticle shadowing can affect reflectance at moderate phase angles (Déau 2015), and either or both could vary with local optical depth in a ring because of local collisional dynamics. As discussed in section 2, further modeling is needed to separate radial (optical-depth-related) variations in the "effective" regolith grain size (Hedman *et al.* 2013) from variations in the macroscopically rough nature of the particles themselves, and the ensuing shadowing effects, or even optical-depth-dependent divergence in layer scattering properties from classical treatments.

The present paper shows, in a simple way, how shadowing effects on spherical albedo can be substantial, but can also be constrained by observational determination of the integrated particle phase function. Such a treatment could remove one level of ambiguity from subsequent analyses, without relying on uncertain forward models, using only knowledge of the particle phase function that comes out of the same analysis that leads to the spherical albedo (see section 1.4 for more discussion). The approach may also be useful in modeling composition of NEOs, where phase functions are well-determined, or even main belt asteroids in many cases (Shevchenko *et al.* 2016, Penttilä *et al.* 2016).

Overview of the paper: After some basic definitions we discuss the reflectance of locally flat, smooth surface elements, and define key parameters and functions (sections 1.1 and 1.2). In section 1.3 we introduce the role of surface roughness and the associated shadowing, and define a key parameter to describe it. In section 1.4 we discuss phase functions for three dimensional particles covered with locally "flat" but "rough" surfaces as discussed above, and show that commonly observed "powerlaw" phase functions are a natural outcome of our simple assumptions.[2] In section 1.5 we discuss the planar albedos of rough flat surfaces and the spherical and geometrical albedos of particles covered by them, and show how to convert an observed spherical albedo, for a rough and shadowed object, to the spherical albedo of an object covered by a smooth, locally flat surface made of the same regolith material (which traditional regolith models can address with less ambiguity). In section 2 we compare our simple model to the full roughness-shadowing forward model of Hapke (1993), finding decent agreement with less dependence on initial assumptions, and mention possible implications for spectral modeling.

1.1 Basic definitions

The reflectance of a resolved surface is typically expressed as I/F, which is the ratio of the observed intensity I (ergs cm^{-2} str^{-1}sec^{-1}) to that of a perfect Lambert disk illuminated at normal incidence by a flux density πF (ergs cm^{-2} sec^{-1}). Cuzzi (1985) presented a discussion and table relating the various photometric properties of flat Lambert and Lommel-Seeliger (LS) surfaces, and the albedo and phase function of a sphere covered with such surfaces. We first define the *planar flux albedo* A_{PF}, or ratio of the total flux reflected by a flat surface (integrated over emergence angles e) to incident flux at incidence angle i, as:[3]

$$A_{PF}(\mu_o) = \int_{-\pi}^{\pi} \int_0^1 \frac{I(\mu, \phi)\mu d\mu d\phi}{\pi F \mu_o}. \tag{1}$$

---

[2]In this paper we discuss macroscopic objects covered by regolith. For clarity we will refer to the macroscopic objects as *particles* and the components of their regolith as *grains*, and use different symbols for their respective albedos.

[3]Hapke (1993) refers to A_{PF} as A_h (hemispherical albedo), or plane albedo, or directional-hemispherical reflectance (his sections 10.E.4 and 10.D.2).
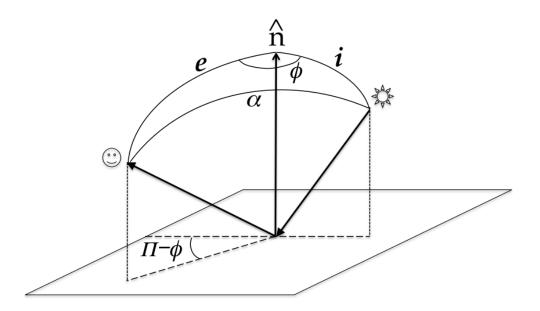
Figure 1: Typical illumination and viewing geometry of a locally flat surface element with surface normal $\hat{n}$. Solar illumination is at incidence angle i, and the viewer is at emission angle e, where $\mu_o = \cos i$ and $\mu = \cos e$. The phase angle α is the angle between the incident and scattered ray, and is given by $\cos\alpha = \mu\mu_o + \cos\phi\sqrt{1-\mu^2}\sqrt{1-\mu_o^2}$.

where $\mu = \cos(e)$, $\mu_o = \cos(i)$, and ϕ is an azimuth angle (**figure 1**). Note that A_{PF} is not the same as *geometric albedo* p (Harris 1961), called A_p by Hapke (1993), which is simply the I/F at zero phase angle (Cuzzi 1985). We define the essential common underlying parameter of our reflectance functions as $\mathcal{R}$, the planar flux albedo of a *macroscopically smooth*, flat, surface element illuminated at normal incidence. For instance, a Lambert surface with $A_{PF} = \mathcal{R}$ has an angle-independent reflected intensity $I/F = \mathcal{R}\mu_o$. We chose this definition of $\mathcal{R}$ because it is independent of surface physical structure and can be measured in the laboratory.

A second important albedo we will use extensively is the *spherical albedo A_s* of an entire particle (also known as the single-scattering albedo):

$$A_s = 2\int_0^1 A_{PF}(\mu_o)\mu_o d\mu_o. \tag{2}$$

For smooth surfaces (**table 1**), there is a simple relationship between $\mathcal{R}$ (the parameter most cleanly constraining composition) and A_s (the parameter most cleanly characterizing particle brightness overall). In general however, it is necessary to retain them both.

1.2 Smooth flat surfaces

Popular smooth, flat surface scattering laws include the Lommel-Seeliger (LS) law (Table 1) and the Lambert law, which is a subset of the Minnaert law:

$$\frac{I}{F} = \frac{\mathcal{R}(1+k)}{2}\mu_o^k\mu^{k-1}, \tag{3}$$

4

where k is the Minnaert parameter and a Lambert surface has $k = 1$. A Lambert law can be theoretically demonstrated to be the high-reflectivity limit of rough particles; see van de Hulst (1957, section 8.42), Lumme and Bowell (1981a), Shkuratov *et al.* (2005), and Muinonen *et al.* (2011). A LS surface has close connections to the single-scattering solution for a traditional diffuse or "classical" many-particle-thick layer, and it has been used often over the years for modeling the moon and various other dark objects (Hapke 1993, Veverka *et al.* 1989, Squyres and Veverka 1981). Counterintuitively, the planar flux albedo $A_{PF}(\mu_o)$ of a macroscopically smooth LS surface with *high assumed* normal reflectivity $A_{PF}(1) = \mathcal{R}$ can exceed unity for small μ_o (see table 1), and the single scattering albedo of a particle covered with such a surface is $A_s = 4\mathcal{R}/3$, which can also exceed unity for $\mathcal{R} > 3/4$ - both nonphysical implications. The fact that $A_s > \mathcal{R}$ for a LS surface becomes more intuitive when one recalls that such a surface does not display its maximum reflectivity at normal viewing. Moreover, since the LS law is the *low-reflectivity*, single-scattering limit for a layer of isotropic scatterers, clearly it would be inconsistent to assign a *high* reflectance $\mathcal{R} > 3/4$ to a LS surface; thus nonphysical magnitudes of A_{PF} and A_s should not be encountered. While a highly reflective surface will simply *not have* the directional properties given by the LS expression, and is best modeled using a Lambert or Minnaert function, the smooth-surface behavior of dark objects should probably be based on the LS law instead of Minnaert surfaces with $k < 1$ for this reason (see section 1.5).

In **figure 2**, we compare the Lommel-Seeliger law with two different scattering laws that are more compatible with bright surfaces. We plot I/F as a function of μ (the cosine of the emission angle) for three different values of μ_o. Dotted lines represent the Minnaert functions. Solid lines represent the classical multiple-scattering result for a semi-infinite layer composed of isotropically scattering monomers: $I/F = S(\mu_o, \mu, \phi)/4\mu = R(\mu_o, \mu, \phi)\mu_o/4(\mu + \mu_o)$ (Chandrasekhar 1960; see figure 1). Using the notation of Hapke (1993), where w_g is regolith grain albedo:

$$\frac{I}{F} = \frac{S(\mu_o, \mu, \phi)}{4\mu} = \frac{w_g \mu_o}{4(\mu_o + \mu)} H(w_g, \mu_o) H(w_g, \mu), \tag{4}$$

where $H(w_g, x)$ is Chandrasekhar's H-function, and for numerical calculations we will adopt the closed-form expression from Hapke (1993, equation 8.57) with $x = \mu$ or μ_o:

$$H(x) = \left[1 - x(1 - \gamma) \left[r_o + \left(1 - \frac{r_o}{2} - x r_o \right) \ln \left(\frac{1+x}{x} \right) \right] \right]^{-1} \tag{5}$$

where $\gamma = \sqrt{1 - w_g}$ and $r_o = (1 - \gamma)/(1 + \gamma)$ (see section 3 for references to these parameters). Different solid curves in figure 2 are for regolith grain albedo w_g = 0.3, 0.6, 0.9, 0.99, and 1.0. It can be seen that, for very low values of w_g, the classical solution approaches the LS law (dashed line assuming $\mathcal{R} = 0.04$). It can also be seen (especially for lower μ_o) that the classical solutions are generally limb bright (brighter as $\mu \to 0$), while the Minnaert solutions (dotted curves) are always limb dark; for the Lambert case ($k = 1$) the reflected brightness is independent of μ. Minnaert solutions with $k \sim 1.1$ are in reasonable agreement with classical solutions for high grain albedos (left and middle panels); however, classical solutions for low incidence angles remain more limb-bright (right panel). In no case would a value of $k > 1.15$ or so be a reasonable match, overall. Minnaert surfaces for $k < 1$ share the properties of the Lommel-Seeliger surface, and are also nonphysical for highly reflective surfaces.

1.3 Rough Flat surfaces:

The above discussion applies to macroscopically smooth, unshadowed surfaces. Unfortunately, even for $k \geq 1$, Minnaert (or classical) layer reflectivities by themselves provide a poor match to the
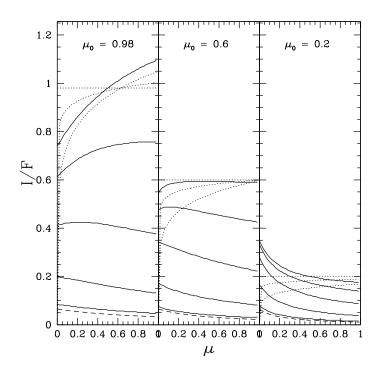
Figure 2: Solid lines: Classical H-function reflectivities I/F for five values of regolith grain albedo w_g = 0.3, 0.6, 0.9, 0.99, and 1.0 (from bottom to top). Dotted lines: Smooth Minnaert surface reflectivities for $\mathcal{R} = 1$ and k = 1.0, 1.05, 1.15 ($k = 1$, the Lambert case, is constant). Dashed line: Lommel-Seeliger reflectivity for $\mathcal{R} = 0.04$.

6

variation of brightness with *phase angle* α (see figure 1) which have been observed for realistic solid objects (*eg.* Dones *et al.* 1993, Pitman *et al.* 2010) or laboratory surfaces (Helfenstein and Shepard 2011, Shepard and Helfenstein 2011).

The most obvious physical attribute lacking from Minnaert and classical layer models is significant macroscopic relief on the target's surface - facets, lumps and holes - and the shadowing thereby created. Relative to a smooth surface, an observer at higher phase angles sees more shadows, and thus a more sharply backward peaked phase function (section 1.4). Harris (1961) presented a version of the Minnaert law with α-dependent $\mathcal{R}$ and k in order to match lunar photometry quantitatively (see also Minnaert 1961). Shkuratov *et al.* (1999) and Kreslavsky *et al.* (2000) adopted a shadowing function of the form $f(\alpha) = \exp(-\mathcal{S}\alpha)$, originally suggested by Akimov (1980), as a prefactor to the smooth-surface reflectance laws, where $\mathcal{S}$ is a roughness parameter. Squyres and Veverka (1981) employed an empirical multicomponent $f(\alpha)$ factor, of which the dominant term is also of the form $\exp(-\mathcal{S}\alpha)$. Hapke (1993) (chapter 12) models this effect from basic geometrical shadowing principles (under various simplifying assumptions), obtaining functions of μ_o and μ multiplied by terms with more complicated functions of α. Goguen *et al.* (2010) related $\mathcal{S}$ (in our notation) to a different physical model of slopes, and Shkuratov *et al.* (2005) models blocky lumps (for more discussion see these articles and references therein). None of the roughness/shadowing models can really distinguish the lengthscale over which roughness and shadowing acts, but comparisons of theoretical and experimental work (Shepard and Helfenstein 2011, Helfenstein and Shepard 2011) suggest the relevant scale is small - mm to cm.

We find the heritage and simplicity of this form of prefactor shadowing correction appealing, and in fact below we show that, in combination with a flat facet reflectance law as simple as Lambertian, it captures much of the observed behavior of ring particle (and icy moon) phase functions. Here, we will explore two forms:

$$f(\alpha) = \exp(-\mathcal{S}\alpha) \quad \text{and} \quad f(\alpha) = \exp(-\mathcal{S}\sqrt{\tan(\alpha/2)}). \tag{6}$$

We will refer to the first expression in equation 6 as the "simple exponential" form. The second expression is functionally similar to, but much simpler than, that derived by Hapke (1993), which matches the best-observed phase functions somewhat better than the simple exponentials used by Kreslavsky *et al.* (2000) or Squyres and Veverka (1981) (see section 1.4); we will refer to it as the "Hapke-like" form. Then, for example, the reflectance of a rough, faceted or cratered surface, illuminated at incidence angle $\cos^{-1}(\mu_o)$ from its nominal normal vector, within which the unresolved, locally flat surface elements are Lambertian, is $I/F = f(\alpha)\mathcal{R}\mu_o$.

Plane and spherical albedos for rough particles: For a smooth Minnaert surface ($\mathcal{S} = 0$), $A_{PF}(\mu_o) = \mathcal{R}\mu_o^{k-1} = (A_s(k+1)/2)\mu_o^{k-1}$ (Equation 1, Table 1), and for this case $A_{PF}(\mu_o = 1) = \mathcal{R}$ by definition. When $\mathcal{S} > 0$, the value of $A_{PF}(\mu_o)$ depends on $\mathcal{S}$ as well as $\mathcal{R}$. Taking a shadowed Minnaert surface as an example:

$$A_{PF}(\mu_o, \mathcal{R}, \mathcal{S}) = \frac{\mathcal{R}(1+k)\mu_o^{k-1}}{2\pi} \int_0^{2\pi} \int_0^1 f(\alpha)\mu^k d\mu d\phi. \tag{7}$$

In determining $A_{PF}(\mu_o, \mathcal{R}, \mathcal{S})$, it is necessary to calculate α for each value of μ_o and the integration variables (see figure 1). Then, recalling equation 2, $A_s(\mathcal{R}, \mathcal{S}) = 2 \int_0^1 A_{PF}(\mu_o, \mathcal{R}, \mathcal{S})\mu_o d\mu_o$. Thus as shown in section 1.5, one cannot properly infer the intrinsic surface composition from A_s alone - one must understand the macroscopic surface roughness in order to back out the "smooth-surface" value of $\mathcal{R}$ that regolith radiative transfer models or laboratory observations address, which *can* be related to composition. Below, we show how this can be done.

property	Lambert	Lommel-Seeliger	Minnaert
I/F	$\mathcal{R}\mu_o$	$\frac{\mathcal{R}\mu_o}{2(1-\ln 2)(\mu+\mu_o)}$	$\frac{\mathcal{R}(1+k)}{2}\mu_o^k\mu^{k-1}$
$A_{PF}(\mu_o)$	$\mathcal{R}$	$\frac{\mathcal{R}}{1-\ln 2}[1-\mu_o\ln(\frac{1+\mu_o}{\mu_o})]$	$\mathcal{R}\mu_o^{k-1}$
$P_o(\alpha)$	$\frac{8}{3\pi}[\sin\alpha+(\pi-\alpha)\cos\alpha]$	$\frac{3}{4(1-\ln 2)}[1-\sin\frac{\alpha}{2}\tan\frac{\alpha}{2}\ln\cot\frac{\alpha}{4}]$	-
A_{so}	$\mathcal{R}$	$\frac{4}{3}\mathcal{R}$	$\frac{2}{k+1}\mathcal{R}$

Table 1: Relationships between scattering laws and albedos of different types, for *macroscopically smooth surfaces* ($\mathcal{S} = 0$; Cuzzi 1985). When $\mathcal{S} > 0$, the local surface element reflectivity will be the product of I/F and a function $f(\alpha)$ manifesting surface shadowing, where α is the phase angle. The planar flux albedo A_{PF} and spherical particle albedo A_s shown here, and the geometric albedo p as well, then decrease with increasing $\mathcal{S}$ (figures 5 - 7). We will refer to the values of A_s as shown above, valid for $\mathcal{S}=0$, as A_{so}. For completeness we note that the geometric albedo $p = A_s P(0)/4$ (in Hapke 1993, $p \equiv A_p$). "Smooth surface" phase functions $P_o(\alpha)$ shown here are normalized in the usual way: $\int P d\Omega = 4\pi$. For shadowed surfaces, section 1.4 shows that the full phase function is simply given by $P(\alpha) = f(\alpha)P_o(\alpha)$ (but must be renormalized). Note that the table caption in Cuzzi (1985) mislabels $\mathcal{R}$ as, essentially, the I/F at normal incidence and reflection, which is true only for a smooth Lambert surface.

1.4 Phase functions

Traditional scattering techniques (and unresolved observations) treat particles as points, each having a phase function $P(\alpha)$ where α is the phase angle. In this situation the incident flux density πF is transformed into an emergent intensity by $I(\alpha) = \pi F A_s P(\alpha)$. For an unresolved object, the observed flux is simply divided by the (known or assumed) solid angle of the object to obtain this average intensity. The phase function is independent of azimuth angle about the incident direction, and is normalized over solid angle Ω such that $\int P(\alpha)d\Omega = 2\pi\int_0^\pi P(\alpha)\sin(\alpha)d\alpha = 4\pi$. For isotropic scattering, $P(\alpha) = 1$.

As a side note, such a treatment of particles as points is acceptable when particles are widely separated, which is not a good assumption for most planetary rings. When particles are closely spaced and much larger than the wavelength, it is most appropriate to treat photons as scattering from individual particle surface elements, each having its own scattering law. Monte Carlo approaches such as Salo and Karjalainen (2003), and ray-tracing approaches in general (Porco *et al.* 2008, Ciarniello 2015) can handle limb darkening and shadowing of particles in principle, but sometimes the process is approximated using the "point" phase functions we discuss here. Monte-Carlo or ray-tracing models of actual surface facet scattering are not discussed in this paper, but they can be based directly on rough-facet results such as presented here.

Some smooth, flat surface scattering laws can be directly integrated over the particle surface to obtain closed-form solutions for the phase function of the particle as a whole. The simplest is the Lambert-surface sphere (Salo and Karjalainen 2003): $P_L(\alpha) = (8/3\pi)[\sin\alpha + (\pi - \alpha)\cos\alpha]$. A sphere covered by a Lommel-Seeliger surface also has a closed-form phase function: $P_{LS}(\alpha) = (3/(4(1 - \ln 2))[1-\sin(\alpha/2)\tan(\alpha/2)\ln\cot(\alpha/4)]$. The phase function advocated by Hapke (1993) (equation 10.46, before accounting for the opposition effect near zero phase angle) is essentially an

albedo-weighted combination of P_L and P_{LS} (see section 1.2 for the role of albedo).

Dones *et al.* (1993) proposed a power-law phase function of the form:

$$P(\alpha) = C_n(\pi - \alpha)^n \tag{8}$$

where α is the phase angle, n is a positive constant, generally between 2 and 6 (Dones *et al.* 1993, Doyle *et al.* 1989), C_n is a normalization constant, given by

$$C_n = \frac{2}{\sum_{i=0}^{\infty} c_{ni}} \tag{9}$$

where

$$c_{ni} = \frac{\pi^{2i+n+2}(-1)^i}{(2i+n+2)(2i+1)!}. \tag{10}$$

We should note that, when converted to magnitudes, the powerlaw phase function does not have the near-linear or slightly concave-upwards behavior seen commonly in observed phase curves of atmosphereless bodies, while equations (14) and (15) below do.

Figure 3 shows various phase functions $P(\alpha)$, calculated by numerical integration over the surface of a sphere covered with elements that locally scatter as the product of a Minnaert law depending only on (μ_o, μ), and a shadowing term (equation 6) depending only on α:

$$\frac{I}{F} = f(\alpha)\frac{\mathcal{R}(1+k)}{2}\mu_o^k\mu^{k-1}. \tag{11}$$

To illustrate how easily the roughness effects separate out, we briefly digress on the integration as applied to the shadowed case, which is generally applicable to any stipulated I/F function with the general form of equation (11). The integral over observable surface elements dA is most easily done in photometric coordinates (Minnaert 1961), where β is photometric latitude and λ is photometric longitude; then $dA = \cos\beta d\beta d\lambda$ (on a unit sphere), and:

$$P(\alpha) = Cc_{\mathcal{S}} \int_{-\pi/2}^{\pi/2} \int_{-(\pi/2-\alpha)}^{\pi/2} I(\mu_o, \mu, \alpha)\cos\beta d\beta d\lambda, \tag{12}$$

where C is the normalization constant for the smooth-surfaced object. We call out a shadowing-related normalization factor $c_{\mathcal{S}}$ separately, as it enters only when $\mathcal{S} > 0$, and only in the phase function. As noted by Harris (1961), the simplification is that for each integration in photometric coordinates at some α, α is *constant across the lit face*, allowing us to take $f(\alpha)$ out of the integral.

From solid geometry[4], $\mu_o = \cos(i) = \cos\beta\cos(\alpha - \lambda)$, and $\mu = \cos(e) = \cos\beta\cos\lambda$. For the Minnaert case this results in

$$P(\alpha) = c_{\mathcal{S}}f(\alpha)C' \int_{-\pi/2}^{\pi/2} \cos^{2k+1}\beta d\beta \int_{-(\pi/2-\alpha)}^{\pi/2} \cos^k\lambda\cos^k(\alpha - \lambda)d\lambda, \tag{13}$$

where the shadowing function $f(\alpha)$ comes out of the integral because α is formally independent of β and λ (see figure 1), and all other constants are lumped into C'. The integral over β can be lumped with C' into a new constant C'', because it is also independent of α. The remaining integral over λ can easily be done numerically, or, for the Lambert case $k = 1$, analytically, providing a handy check on the numerics. For the more complicated H-function-derived I/F, or any other function in general,

---

[4]The sign convention for λ in Hapke (1993, p. 111) is opposite to ours.

$\mathcal{S}$	$c_{\mathcal{S}LE}$	$c_{\mathcal{S}LH}$	$c_{\mathcal{S}LSE}$	$c_{\mathcal{S}LSH}$
0.0	1.00	1.00	1.00	1.00
0.2	1.23	1.16	1.25	1.17
0.4	1.49	1.35	1.53	1.37
0.6	1.79	1.56	1.86	1.60
0.8	2.14	1.80	2.24	1.86
1.0	2.52	2.08	2.67	2.15
1.2	2.96	2.39	3.15	2.48
1.4	3.44	2.73	3.69	2.86
1.6	3.97	3.13	4.28	3.28
1.8	4.55	3.57	4.93	3.77

Table 2: The normalization constant $c_{\mathcal{S}}$ for a range of $\mathcal{S}$. Subscript L refers to an underlying Lambert phase function (equation 14), and subscript LS refers to an underlying Lommel-Seeliger phase function (equation 15). Subscript E refers to the simple exponential $f(\alpha)$ (first expression of equation 6) and subscript H refers to the Hapke-like $f(\alpha)$ (second expression of equation 6).

a tabular lookup can be used to get values of (μ_o, μ) uniquely from each (β, λ). The constant C'' is determined by normalizing the *smooth surface* ($\mathcal{S} = 0$, $c_{\mathcal{S}} = 1$) phase function: $\int P_o(\alpha)d\Omega = 4\pi$. The fact that $f(\alpha)$ comes out of the integrals makes it possible to write the combined spherical phase function for a shadowed Lambert or LS surface (Hapke (1993, equation 12.59); Squyres and Veverka (1981)) directly as:

$$P_{S-L}(\alpha) = c_{\mathcal{S}}f(\alpha) \cdot \frac{8}{3\pi}[\sin\alpha + (\pi - \alpha)\cos\alpha] = c_{\mathcal{S}}f(\alpha)P_{o-L}(\alpha), \qquad (14)$$

or

$$P_{S-LS}(\alpha) = c_{\mathcal{S}}f(\alpha) \cdot \frac{3}{4(1 - \ln 2)}[1 - \sin\frac{\alpha}{2}\tan\frac{\alpha}{2}\ln\cot\frac{\alpha}{4}] = c_{\mathcal{S}}f(\alpha)P_{o-LS}(\alpha), \qquad (15)$$

where the closed-form expressions for P_{o-L} and P_{o-LS} are properly normalized in table 1 when $\mathcal{S} = 0$; when $\mathcal{S} > 0$ a further normalization for each phase function $2\pi c_{\mathcal{S}} \int f(\alpha)P_{o-L}(\alpha)\sin\alpha d\alpha = 4\pi$ is needed (see Table 2). So the smooth *or rough* particle phase functions are determined by the surface element scattering law (I/F, first row in Table 1 when $\mathcal{S}$=0) for an individual facet.

Various typical (normalized) phase functions are shown in **figure 3**, in two formats to make the high- and low-phase behavior equally visible. The clusters of solid lines contain curves for Minnaert $k = 1.0, 1.05, 1.15$ respectively; this variation of k produces negligible difference in the phase functions. These different clusters are separated by their shadowing parameter $\mathcal{S}$ = 0.0 (bottom set), 0.6, 1.0, and 1.4. A shadowed Lommel-Seeliger particle phase function is shown in the blue dotted lines, for $\mathcal{S}$ = 0, 0.8 (left), and 1.4 (right). The colored dashed lines are for a Lambert sphere (red), and the best-fit powerlaw phase functions cited by Dones *et al.* (1993) for Europa (cyan) and Callisto (Doyle *et al.* 1989, Dones *et al.* 1993 (green)). The shadowed-Minnaert functions provide quite a good match to observed powerlaw phase functions over the relevant range; the shadowed Lommel-Seeliger provides as good a fit at low phase angles, but a less good fit at high phase angles, and lacks physical justification for bright particles. The single-scattering shadowed phase function of Lumme and Bowell (1981b, equation 27) is of a very similar form to our "Hapke-like" $f(\alpha)$ alone; however instead of multiplying a Lambert phase function it is additive.

For additional reference we show in **figure 4** a grid of shadowed-Lambert particle phase functions (Minnaert $k = 1$), using either the simple exponential form (solid curves) or Hapke-like form
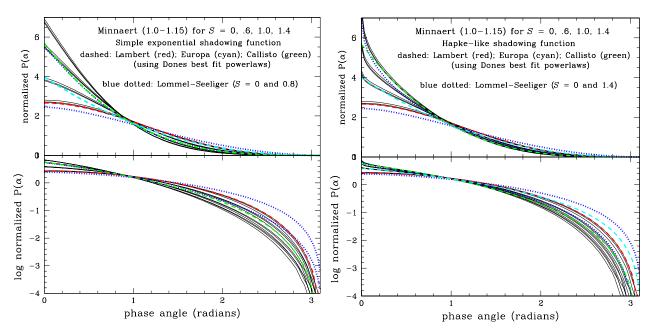
Figure 3: Typical shapes of phase functions for Europa (cyan dashed) and Callisto (green dashed, n=3.3 powerlaw) are fairly well matched by different choices of the shadowing parameter $\mathcal{S}$ in equation 6; Callisto is apparently photometrically rougher than Europa. The red dashed line is an unshadowed Lambert surface. Solid curves are families of Minnaert functions (of which the Lambert case is a subset) with different $\mathcal{S}$, and the blue dotted curves are similarly treated LS functions. Left: simple exponential $f(\alpha) = \exp(-\mathcal{S}\alpha)$; Right: Hapke-like $f(\alpha) = \exp(-\mathcal{S}\sqrt{\tan(\alpha/2)})$.

(dashed curves) of $f(\alpha)$ (equation 6), along with best-fitting powerlaw phase functions for Europa, Callisto, and Saturn's ring particles, and phase functions digitized from Pitman *et al.* (2010) for Rhea in two near-IR bands. In their overall shape, the observations seem to favor the Hapke-like $f(\alpha)$.

It is intriguing that the product of even our simple exponential shadowing function (equation 6) and either the Lommel-Seeliger or Minnaert surface scattering law, results in particle phase functions that agree with the powerlaw phase functions $P_n(\alpha) = c_n(\pi - \alpha)^n$ advocated on purely empirical grounds by Dones *et al.* (1993) for ring particles and other satellite and lunar phase curves, which display a concave-upwards dependence on phase angle. Indeed this agreement strikes us as providing some degree of physical justification previously lacking for the arbitrarily chosen powerlaw expression. Nevertheless, as noted above, our equations (14) and (15) have a shape more closely resembling actual phase functions (shape differences are most apparent when converted to magnitudes).

For completeness, we note in the context of planetary rings, that "particle phase functions" backed out of observations of ring I/F to date have invariably assumed the traditional "Chandrasekhar" formalism for the scattering behavior of the layer as a whole, or at least a formalism in which $P(\alpha)$ factors out (Doyle *et al.* 1989, Dones *et al.* 1993, Cuzzi and Estrada 1998, Cuzzi *et al.* 2002, Bradley *et al.* 2013, Déau 2015, Ciarniello 2015). However, this approach forces $P(\alpha)$ to absorb *whatever nonclassical behavior is not properly handled by the "Chandrasekhar" formalism.* In the case of Doyle *et al.* (1989) and Dones *et al.* (1993), powerlaw phase functions were adopted that automatically go to zero at high phase angles. However, Déau (2015) obtain $P(\alpha)$ empirically for the B ring and C Ring, by backing out the Chandrasekhar layer function. After normalization, these phase functions are in good agreement with each other; however, both have significant "isotropic" contributions and do not go to zero at high phase angles, as do phase functions observed previously for the C Ring
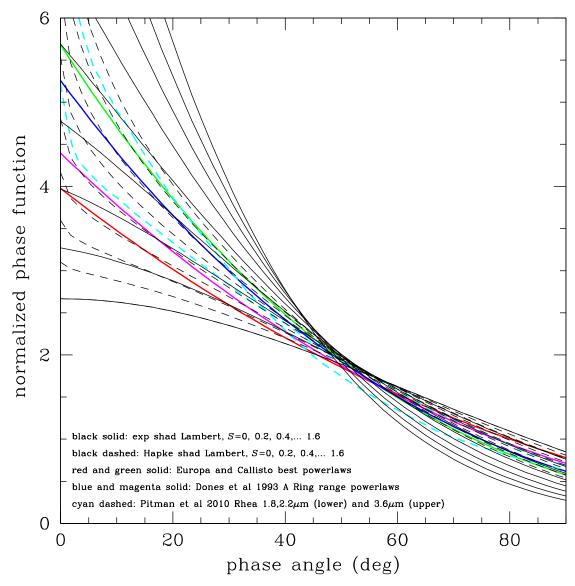
Figure 4: A low-phase-angle closeup of a grid of shadowed-Lambert phase functions using the simple exponential form (solid curves) or Hapke-like form (dashed curves) of $f(\alpha)$, for $\mathcal{S} = 0.0$ to 1.4 in increments of 0.2. We also show best-fitting powerlaw phase functions for Europa (red), Callisto (green), and ring particles (magenta and blue) from Dones *et al.* (1993) and our digitization of observed phase functions from Pitman *et al.* (2010) for Rhea (cyan dashed curves) in two near-IR bands: 1.8μm and 2.2μm (lower), where Rhea is bright in the continuum away from any water ice bands, and at 3.6μm (upper), deep in a strong ice band where Rhea is very dark. The observations seem to favor the Hapke-like $f(\alpha)$.
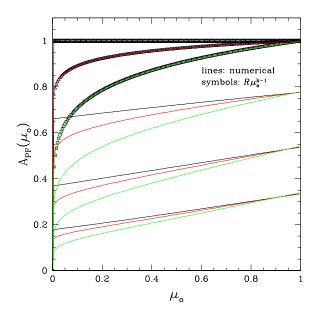
Figure 5: The planar flux albedo A_{PF} for the Hapke-like $f(\alpha) = \exp(-\mathcal{S}\sqrt{\tan(\alpha/2)})$ (equation 6). The curves show $A_{PF}(\mu_o)$ determined numerically for shadowed Minnaert surfaces with $\mathcal{R} = 1$ and k=1.0, 1.05, and 1.15 (black, red, and green) given four values of $\mathcal{S}$= 0, 0.4, 1.0, and 1.8 (groups from top to bottom). The analytical results for $\mathcal{S} = 0$ (see Table 1) are shown by symbols.

(Cooke *et al.* 1991, Cooke 1991) or satellite phase functions (Pitman *et al.* 2010). This might be because the "Chandrasekhar" layer scattering formalism used in this analysis had no way to account for multiple scattering or high optical depth nonidealities which might be important at moderate to high phase angles. Some first order corrections for this nonideality have been presented by Salo and French (2010). In the case of planetary rings, future Monte Carlo models which can handle surface element scattering by realistic rough-surfaced particles, in realistic closely-packed, "nonclassical" layers, will be needed to properly address this distinction.

1.5   Albedos are a function of roughness

Planar Flux albedo: In **figure 5** we show $A_{PF}(\mu_o)$ based on various I/F models for Minnaert functions with $\mathcal{R} = 1$ and k=1.0, 1.05, 1.15 (black, red, green) as shadowed by four values of $\mathcal{S} = 0.0$, 0.4, 1.0, and 1.8. Recall $k = 1$ is the Lambert case where, for $\mathcal{S} = 0$, $A_{PF}(\mu_o) = \mathcal{R}$. All the curves are numerically derived here, but for the top triplet, an unshadowed case or $\mathcal{S}$=0, we also plot the analytical solutions ($A_{PF}(\mu_o) = \mathcal{R}\mu_o^{k-1}$; table 1) as symbols. The agreement is quite good. $A_{PF}(\mu_o = 1)$ decreases with increasing $\mathcal{S}$, even while the surface material is unchanged, because $A_{PF}(\mu_o = 1)$ includes intensity contributions from emergent directions at phase angles away from zero, where shadowing increases as $\mathcal{S}$ increases. $A_{PF}(\mu_o)$ decreases further as μ_o decreases because shadows become even more important at smaller μ_o. While A_{PF} depends on $\mathcal{S}$, we reserve the parameter $\mathcal{R}$ to refer only to the case $\mathcal{S} = 0$ - a granular but macroscopically smooth surface.

Geometric albedo: The geometric albedo $p = A_s P(0)/4$ of an entire macroscopic particle (see Table 1 and Cuzzi 1985) is insensitive to roughness and shadowing because shadowing is not
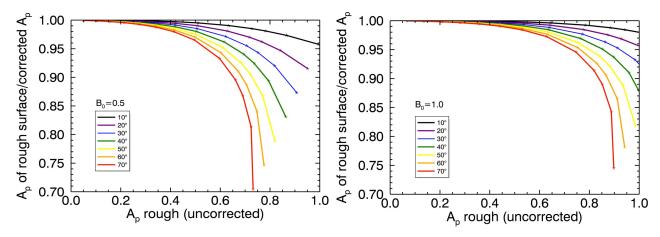
13

Figure 6: Correction to the geometric albedo A_p for the effect of roughness, as a function of observed A_p for several Hapke $\bar{\theta}$ values. In determining A_p, it is assumed that the opposition surge is due to shadow hiding only. Left: opposition surge amplitude B_o=0.5; Right: opposition surge amplitude B_o=1.0. These models assume a regolith grain single-lobed Henyey-Greenstein phase function with asymmetry parameter =-0.3; higher A_p values can be obtained for more backscattering grains (-0.5).

significant at phase angles less than about 10-20 degrees (Helfenstein and Shepard 2011, Shepard and Helfenstein 2011). However, the correction is not entirely negligible, and can be important for very bright surfaces, so needs to be addressed if quantitative compositional inferences are to be drawn. We show the effect by calculating Hapke's (1993) *smooth surface* geometric albedo (Hapke calls geometric albedo A_p) over a range of regolith grain albedo w_g, using his equations 8.22b, 8.25, and 10.38, and then converting this value of A_p to that of a *rough, shadowed* surface using Hapke's (1993) "U function" (his equations 12.58 and 12.60) for different values of his slope parameter $\bar{\theta}$. We plot the ratio of the rough surface A_p to the smooth surface A_p in **figure 6**, as a function of the rough surface (observed) A_p. Each color represents a different $\bar{\theta}$, and the symbols along each curve represent different w_g. The corrections are generally small (<20%) except for bright objects with very macroscopically rough surfaces. However, Hapke (1993) admits that the theory is questionable for very bright surfaces, because illumination of facets by other facets is neglected, and *also* for very large $\bar{\theta}$ because high order terms have been neglected. So overall, not surprisingly, geometric albedos are not sensitive to roughness and shadowing.

While working with A_p (or p) thus has some advantages, the strong opposition effect (especially for bright objects such as Saturn's rings) complicates matters (French *et al.* 2007, Salo and French 2010, Verbiscer *et al.* 2013; compare figures 6 left and right). There is considerable ongoing uncertainty into the nature of the opposition effect(s) and how to properly model it (them); for recent discussions see Muinonen *et al.* (2011) or Déau *et al.* (2013). Because of this uncertainty and the minor influence of the opposition effects on the integrated reflected energy balance (they contribute over a very small solid angle), we will emphasize an approach to compositional inference centered on the spherical (or single-scattering) albedo A_s and avoiding extremely small α. Deemphasizing the opposition effect is consistent with our reliance on Hapke (1993) instead of Hapke (2012), which differs primarily in adding more complicated treatments of coherent backscattering.

Spherical albedo: The particle's spherical albedo A_s (equation 2) depends on *both* its composition (as manifested in $\mathcal{R}$, which one can envision measuring or modeling for a grainy but macroscopically smooth surface) *and* its macroscopic roughness (as manifested in $\mathcal{S}$). This effect can be understood by taking a smooth surfaced particle of some composition, and roughening the surface so

shadows are seen at all phase angles greater than zero. Except in the opposition surge near $\alpha = 0$, the rough particle appears less bright at all phase angles than a smooth one of the same composition because of the shadows, so has a lower value of A_s overall. It is not possible to infer compositional information from A_s alone, without knowing the associated value of $\mathcal{S}$. While Hapke (1993) discusses the shadowing effect in chapter 12 of his monograph, he does not provide an explicit correction for A_s (see section 2 however).

Figure 7 shows how the particle spherical albedo A_s varies with shadowing parameter $\mathcal{S}$ for both shadowing laws in equation (6). Both shadowed-Minnaert and shadowed-H-function curves appear in this diagram. The Minnaert curves all assume $\mathcal{R} = 1$, and the $\mathcal{S}$=0 values would scale linearly with $\mathcal{R}$. In the left panel, we show actual spherical albedos from our model for objects with either different Minnaert k, or as computed for different grain albedos w_g using the H-function approach of Hapke theory (equations 4 and 5). More absorbing material, naturally, leads to lower w_g, and thus lower smooth surface ($\mathcal{S} = 0$) spherical albedos; meanwhile, roughness (increasing $\mathcal{S}$) decreases these albedos further.

The curves in the right hand panel show the rough surface albedos normalized by their $\mathcal{S} = 0$ equivalent value A_{so}. Surprisingly, they collapse onto a single, essentially albedo-independent family for each $f(\alpha)$ which can be approximated by very simple functions $\xi(\mathcal{S}) \equiv A_s/A_{so}$ (magenta and blue heavy curves in right panel). This behavior makes it very easy to apply the surface roughness correction. The ratio $\xi(\mathcal{S})$ can be thought of as a way of correcting the *observed* spherical albedo for a rough, lumpy particle to the spherical albedo for a particle made of *the same granular material* if its surface were smoothed out. The near-invariance of the $\xi(\mathcal{S})$ function with grain albedo w_g (for a given $f(\alpha)$) means that the *shape* of the underlying "smooth-surface" phase function plays a minor role, even while it changes from a Lommel-Seeliger law to a Lambert law as w_g varies from 0 to 1 (equation 10.46 of Hapke 1993, and figures 2 and 3).

All values of observed A_s lying on the (closely spaced cluster of) Minnaert curves in figure 7 (left; dotted lines, for k=1.0, 1.05, 1.15) refer to particles for which a smooth surface would have $\mathcal{R} \approx 1$! Yet, depending on roughness, even these highly reflective materials can have much lower A_{PF} (figure 5), and A_s (figure 7). Uncorrected roughness and shadowing will lead one to overestimate the amount of intrinsic absorptive material present. This implication is supported by the H-function curves, each for a different grain albedo w_g (left panel of figure 7). Lower grain albedos w_g, of course, produce darker regoliths (lower A_{so}), and the grain albedo w_g *is* directly linked to particle composition. However, A_s can also be reduced by increasing $\mathcal{S}$. Note there is no "imposed" normalization here of $A_{PF}(\mu_o)$ or A_s associated with $\mathcal{S}$. Only the phase function is renormalized for different values of $\mathcal{S}$, as in Hapke (1993).

The collapse of the curves in figure 7 (right), for all values of intrinsic surface absorptivity as controlled by w_g, does not imply that any combination of $\mathcal{R}$ and $\mathcal{S}$ is possible. As alluded to earlier, if one created a particle from material that truly does not absorb light, both A_s and w_g must be unity (thus also $\mathcal{R}$), and so it *could not have* a phase function characterized by strong shadowing (a steep powerlaw, or $\mathcal{S} > 0$). If the surface is non-absorbing, photons scattered away from lit surface elements would illuminate directly shadowed ones and return to space. As discussed in van de Hulst (1957) (section 8.42), the so-called "Schönberg sphere", a perfectly reflecting, very rough particle, has the phase function of a Lambert sphere (that is, $k = 1$, $\mathcal{R} = 1$, and $\mathcal{S} = 0$).

Some support for this comes from observational, experimental, and theoretical studies. $\mathcal{S}$ associated with Europa is lower than with Callisto (figure 3), and the A_s-dependent trend of $\mathcal{S}$ evident from figure 7 and tables 9 and 10 of Pitman *et al.* (2010) for Rhea (Rhea's phase curves become steeper and more concave upward with decreasing albedo as wavelength is varied). Phase curves for darker asteroids are steeper than those for brighter ones (Shevchenko *et al.* 2016, Penttilä *et al.* 2016). Also,
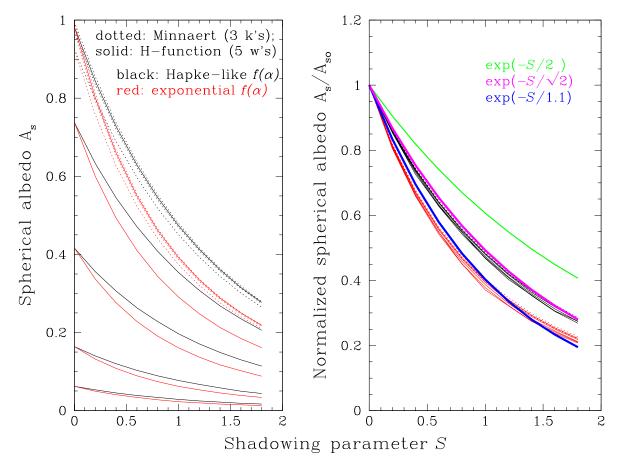
Figure 7: **Left:** Spherical albedo A_s as a function of roughness/shadowing parameter $\mathcal{S}$ for two different surface shadowing laws $f(\alpha)$: exponential (red; equation 6 left) and Hapke-like (black; equation 6 right). Dotted curves of each color: Minnaert facet laws using $k = 1.0, 1.05, 1.15$ and $\mathcal{R} = 1$; solid curves of each color: H-function models with w_g= 0.3, 0.6, 0.9, 0.99, and 1.0 (w_g values increase upward). Increased roughness and shadowing decrease the spherical albedo significantly. **Right:** Here, all curves shown in the left panel are normalized by their $\mathcal{S} = 0$ value, defining the function $A_s/A_{so} \equiv \xi(\mathcal{S})$. The curves for a Hapke-like $f(\alpha)$ collapse into an $\mathcal{R}$-and-w_g-independent cluster (black curves) well represented by $\xi(\mathcal{S}) = \exp(-\mathcal{S}/\sqrt{2})$ (heavy magenta curve); the curves for a simple exponential $f(\alpha)$ also collapse (red cluster) and are approximated by $\xi(\mathcal{S}) = \exp(-\mathcal{S}/1.1)$ (heavy blue curve). This difference gives an estimate of the uncertainty in the correction from observed (rough) to smooth particle albedo. The value of $\mathcal{S}$ inferred from observations might differ depending on the form of $f(\alpha)$. The fact that the H-function albedo corrections collapse so well over a wide range of grain spherical (single-scattering) albedo w_g testifies to the insensitivity of the technique to the assumed smooth surface scattering law (Lambert or L-S).
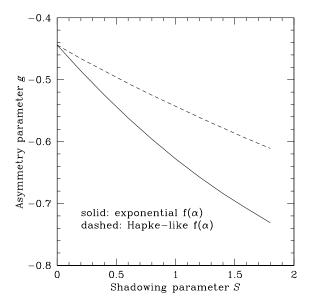
16

Figure 8: The scattering asymmetry parameter g (equation 16) for shadowed-Lambert phase functions as defined in equation 14 and seen in figures 3 and 4, using the two shadowing functions $f(\alpha)$ defined in equation 6.

Pilorget *et al.* (2016) see just this effect in the lab (their figure 9 most clearly shows the anticorrelation between grain albedo and inferred roughness in the sense of mean facet slope). Finally, Muinonen *et al.* (2011) see nearly Lambertian scattering ($\mathcal{S}$=0) for very rough surfaces, if they are also bright. Muinonen *et al.* (2011) and Pilorget *et al.* (2016) ascribe their results to multiple inter-grain or facet scattering. This behavior is built in to the shadowing theories of Lumme and Bowell (1981a,b) and Shkuratov *et al.* (1999, their equation 28*ff*) but not that of Hapke (1993, chapter 12).

We note a crude, but systematic, way to connect arbitrary observational phase functions with the rough-smooth albedo correction of figure 7 (right), as long as their scattering asymmetry parameter g is known. **Figure 8** shows the asymmetry parameter

$$g = \langle \cos\Theta \rangle = \frac{\int_0^\pi P(\Theta)\cos\Theta\sin\Theta d\Theta}{\int_0^\pi P(\Theta)\sin\Theta d\Theta}. \tag{16}$$

(where $\Theta = \pi - \alpha$), as a function of $\mathcal{S}$, for shadowed-Lambert phase functions with the two forms of $f(\alpha)$ given in equation 6. For any phase function of arbitrary shape with known g, figure 8 provides a value of $\mathcal{S}$ which can be used in figure 7 to at least estimate the rough-to-smooth-surface correction factor.

For reference in section 2, we also note at this point the traditional relationship $A_s \equiv pq$ (Hapke 1993, eq. 10.54), where the phase integral q is defined as

$$q = 2 \int_0^\pi \frac{P(\alpha)}{P(0)}\sin\alpha d\alpha. \tag{17}$$

2 Comparison with rough-particle theory of Hapke (1993)

Hapke (1993) has developed an elaborate, first-principles, essentially geometric-shadowing-based forward model of the effect of surface roughness on surface brightness. The theory, laid out in chapter 12 of his monograph, will not be reiterated here and we will simply reference relevant equations. Hapke's development results in multiplicative functions that can be applied to convert "smooth-surface" reflectivities into "rough-surface" reflectivities. The conversion functions depend on phase angle α (called g in Hapke 1993) and a slope parameter $\overline{\theta}$, and include numerical factors chosen to give good agreement with a variety of planetary surfaces. One such function $K(\alpha, \overline{\theta})$ converts the phase function of a nominally spherical, regolith-covered object with a *smooth* surface - $P_o(\alpha)$ in our notation or $\Phi(\alpha, w_g, 0)$ in Hapke's notation[5] - into the phase function $P(\alpha, \overline{\theta})$ (or $\Phi(\alpha, w_g, \overline{\theta})$) of an object made of the same granular material, but with a roughened surface covered by unresolved facets and craters:

$$P(\alpha, \overline{\theta}) = P_o(\alpha)K(\alpha, \overline{\theta}), \tag{18}$$

where Hapke (1993) tabulates $K(\alpha, \overline{\theta})$, but says that for phase angles less than $60°$ it can be approximated by

$$K(\alpha, \overline{\theta}) = \exp\left[-0.32\overline{\theta}(\tan\overline{\theta}\tan(\alpha/2))^{1/2} - 0.52\overline{\theta}\tan\overline{\theta}\tan(\alpha/2)\right] \tag{19}$$

Note that in the formulation of Hapke (1993) the smooth surface particle phase function $\Phi(\alpha, w_g, 0)$ itself is a function of regolith grain albedo w_g in a forward-modeling sense, whereas in our model there is no explicit dependence. Instead, we work backwards from a phase function that is determined by observations, assuming the rough surface shadowing correction operates on a smooth-surface phase function that is nearly Lambertian (it could be Minnaert or Lommel-Seeliger with little effect).

Comparing equations (14) and (18) shows that Hapke's $K(\alpha, \overline{\theta})$ plays the same role as our function $f(\alpha)$ (equation 6): both multiply a smooth surface particle phase function. In our model, the smooth particle is assumed to have a composition-independent Lambertian phase function characterized by a surface element planar flux albedo $\mathcal{R}$ and a corresponding spherical albedo A_{so} (Table 1). One can then model $\mathcal{R}$ or A_{so} separately using traditional Hapke, Shkuratov, or van de Hulst type granular regolith radiative transfer models while neglecting explicit roughness effects (*eg.* equation 10.51b of Hapke 1993).

A comparison between our (normalized) results (right panel of figure 7) and those obtained from the complete Hapke theory is shown in **figure 9**. The Hapke results are shown in the symbols, one set for each grain albedo w_g= 0.1 - 0.99, with 0.99 being the lowest at each value of $\mathcal{S}$. Hapke (1993) does not give a direct correction of spherical albedo A_s for roughness and shadowing. Thus, to calculate a *rough, shadowed* particle spherical albedo as a function of his roughness parameter $\overline{\theta}$, we start with his smooth particle *geometric* albedo A_p and use its roughness correction function $U(\overline{\theta})$ to determine the geometric albedo of a rough particle as described in section 1.5. Both A_p and $U(\overline{\theta})$ are parameterized by w_g. We also determine the phase integral q (equation 17 above) from the *rough* surface phase function, which is (for this test) corrected from Hapke's *smooth* surface phase function $\Phi(\alpha, w_g, 0)$ using his $K(\alpha, \overline{\theta})$ function (eqs. 12.59 and 12.61).[6] $K(\alpha, \overline{\theta})$ does not depend on w_g, but

---

[5]Hapke's $\Phi(\alpha, w_g, 0)$ has a different normalization than our $P_o(\alpha)$, being normalized to its zero-phase value.

[6]To be more specific, we use Hapke's equations 8.22b, 8.25, and 10.38 (which assumes 8.56) for A_p and quantities going into it, all of which enter into his equation 10.47 (with 8.90) for $\Phi(\alpha, w_g, 0)$. We assume an opposition surge due to shadow-hiding only, with an angular width h of 0.3, but one could ignore the opposition effect as it contains negligible scattered energy. In realistic cases, the grain albedo w_g can be a volume average (Hapke 1993, eqn 7.45a) where for a given grain with intramixed "pollutants", refractive indices are obtained using effective medium theory (Cuzzi *et al.* 2014). Hypothetical, nonisotropic regolith grain phase functions (Souchon *et al.* 2011) can be treated using similarity relations (equations 10.25a and b of Hapke 1993), as discussed in section 3. None of these complications regarding realistic materials are used in this paper, where we simply assume a range of w_g, but we note the thread for the convenience of the reader.
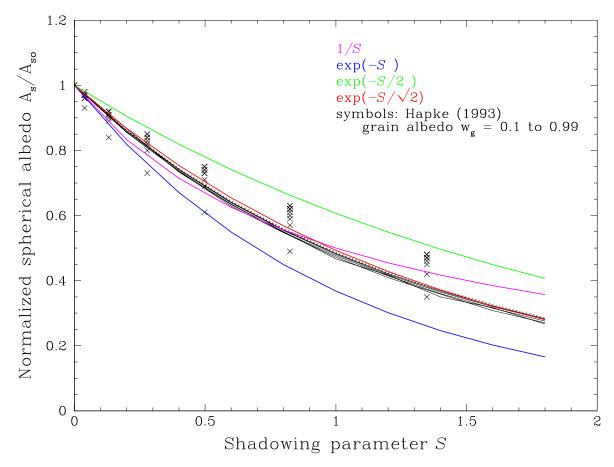
Figure 9: Comparison of the shadowing effects on particle spherical albedo A_s, from our simple model (curves, taken from figure 7) and from the forward model of Hapke (1993) (symbols, for w_g ranging downwards from 0.1 to 0.99 at each value of $\mathcal{S}$). The approach is explained in section 2. Overall the agreement is fairly good; our model is much less sensitive to composition.

$\Phi(\alpha, w_g, 0)$ does. We then calculate $A_s = A_p q$ to determine the spherical albedo of a rough particle. In order to make the direct comparison of models shown in figure 9, we slightly distorted the second term in the exact form of Hapke's $K(\alpha, \overline{\theta})$ so that its functional form is identical to the first term:

$$K(\alpha, \overline{\theta}) = \exp\left[-0.32\overline{\theta}(\tan\overline{\theta}\tan(\alpha/2))^{1/2} - 0.52\overline{\theta}(\tan\overline{\theta}\tan(\alpha/2))^{1/2}\right] \qquad (20)$$

Comparing this form with our own $f(\alpha)$ we see that $\mathcal{S} \approx 0.84\overline{\theta}\sqrt{\tan\overline{\theta}}$; this allows us to compare our predictions for A_s/A_{so} (parameterized by $\mathcal{S}$) directly with those we infer from Hapke (parameterized by $\overline{\theta}$). The general overlap between the two solutions is encouraging, given the simplicity of our approach and the various approximations in the approach of Hapke (1993). Even the functional form of equation (19), which we have distorted in equation (20) to have the same α dependence as equation (6), is only claimed as a good fit by Hapke (1993) for phase angles less than $60°$. The decent agreement seen in figure 9 is probably due to the fact that, for objects with phase functions such as these, most of the energy is scattered at low and moderate phase angle.

Before closing, we note that the effect described here - a necessary correction from rough-surface to smooth-surface spherical albedo prior to compositional modeling - may have implications

for compositional inferences from *spectral band shape modeling* as well. Consider an absorption band in the observed I/F of an icy surface, and assume that geometrical and layer effects can be properly removed in converting I/F to A_s. Figure 7 shows that surfaces of larger $\mathcal{S}$ require a larger correction to obtain "smooth-surface" A_{so}. We have argued that rough particles made of intrisically dark, absorbing material may have phase functions characterized by systematically larger values of $\mathcal{S}$ compared to comparably rough but highly reflective surfaces (end of section 1.5). This suggestion is amenable to simple experimental testing. Thus it is likely that the appropriate *rough-to-smooth correction* is systematically larger for more absorbing surfaces (thus, larger in the depths of a band than in the nearby continuum). This means that absorption features - even in a single composition surface such as the icy surfaces of the rings and moons of the outer solar system - may appear artificially deep when observed well away from opposition, causing uncorrected "rough-surface" albedos obtained from them to exaggerate the inferred grain size, *especially* in ice-rich surfaces where the spectral contrast is largest. For example, it has been reported that the regolith grain size is larger in the A and B rings than in the C Ring (see a recent review by Cuzzi *et al.* 2009), and even perhaps that the A Ring regolith grains are slightly larger than those on B Ring particles. Yet, this is just the sort of systematic bias that one might expect from uncorrected shadowing if the A Ring particles were, for whatever reason, rougher-surfaced or clumpier. More study is needed to see if the regolith grain size effect is real or not.

3   Cookbook approach to applying the technique:

(a) In practice, one first obtains the observed (rough particle) spherical albedo A_s and phase function $P(\alpha)$ by measuring the brightness as a function of phase angle α, from observations over a range of geometries (figure 3). For an isolated object, the fit for the phase function is straightforward. For a ring system of optical depth τ, this step usually involves fitting the so-called 'Chandrasekhar' or classical, single-scattering expression

$$I/F = \frac{A_s P(\alpha)\mu_o}{4(\mu_o + \mu)} \left[1 - \exp\left(\frac{-\tau(\mu_o + \mu)}{\mu_o\mu} \right) \right],\tag{21}$$

to a collection of observations at different α, μ_o, and μ values. It should be remembered that any deviation of the *actual* layer reflectivity function from equation 21, including a significant multiple scattering contribution or closely packed particles, will lead to a distortion of the inferred phase function $P(\alpha)$ (for more discussion see Cuzzi *et al.* 2002, Salo and French 2010, and section 1.4 above).

(b) Either way, $\mathcal{S}$ is then determined by matching the *shape* of the particle's observed phase function to equation 14 or 15. If unknown, the phase variation can be assumed by analogy with similar objects (introducing uncertainty, of course).

(c) One next corrects A_s for shadowing, using one of the collapsed normalized (blue or magenta) curves of figure 7 (right) which we call $\xi(\mathcal{S})$. The *smooth particle spherical albedo* $A_{so} \equiv A_s(\mathcal{S} = 0)$ is given by $A_{so} = A_s/\xi(\mathcal{S})$. For the Lambert surface facets underlying figure 7, we can identify $\mathcal{R} = A_{so}$ (Table 1). This *observationally determined* A_{so} can then be compared with various *theoretical model* values for smooth-surfaced particles of different composition, as described in the following steps.

(d) The first step in modeling A_{so} is to get the grain albedo w_g, which depends only on the grain radius and refractive indices; see Hapke (1993, chapter 6), Cuzzi and Estrada (1998, equations 2-5), Hendrix and Hansen (2008, equations 2-3), or Shkuratov *et al.* (1999) as discussed by Poulet *et al.* (2002). The refractive indices can be just taken for the pure material, or an "intramixture" of material

within a single grain can be approximated by a volume-fractional blend (Cuzzi and Estrada 1998) or obtained more accurately using Effective Mixture Theory (Cuzzi *et al.* 2014). An average value of w_g for an "intimate mixture" of grains having different compositions can be calculated as in Roush (1994).

(e) The following basic parameters are determined from w_g using equations 8.22b and 8.25 of Hapke (1993), assuming isotropically scattering regolith grains of albedo w_g:

$$\gamma = \sqrt{1 - w_g} \quad \text{and} \quad r_o = \frac{1 - \gamma}{1 + \gamma}. \tag{22}$$

(f) The approaches we use below are based to varying degrees on isotropically scattering re-golith grains.[7] **In general the regolith grain phase function $P_g(\alpha)$ is approximated by a Henyey-Greenstein phase function: $P_g(\alpha) = (1 - g^2)/(1 + g^2 - 2g\cos\alpha)^{3/2}$, where g is the the scattering asymmetry parameter (equation 16 above and equation 6.7 of Hapke 1993). This phase function is normalized in the usual way such that for isotropic scattering, $P_g(\alpha) = 1$.** The Hapke theory does not *calculate* a grain scattering asymmetry factor g, nor does it include diffraction of the scattered light in w_g as does Mie theory. However, even without diffraction, the reflected and transmitted light *are already* significantly anisotropic for transparent, icy grains and even for the dielectric slabs on which the Hapke w_g are based (Liou and Hansen 1971, Liou *et al.* 1983). Poulet *et al.* (2002) show how an effective g can be derived from the model of Shkuratov *et al.* (1999), or a range of g values can simply be assumed (Hapke 1993, chapter 6 **and figure 6.9**). We model anisotropic grain scattering phase functions in several ways (see g1-g3 below). The so-called "similarity relations" convert the albedo of a nonisotropic scatterer into that of an isotropic scatterer. That is, the directly calculated w_g can be combined with any assumed asymmetry parameter g into an "effective" value w_{gi} for an isotropically scattering grain using equation (14) of van de Hulst (1974), as adopted by Hapke (1993, his equation 10.25a):

$$w_{gi} = w_g \left(\frac{1 - g}{1 - gw_g} \right). \tag{23}$$

Substituting w_{gi} back into equation 22 above, we get

$$\gamma_i = \left(\frac{1 - w_g}{1 - gw_g} \right)^{1/2}. \tag{24}$$

This "effective isotropic" value of γ, and if needed, the associated value of r_o, can be used in any of the techniques below to get the spherical albedo A_{so} for a smooth particle covered in regolith grains with albedo w_g and asymmetry parameter g. The basic similarity relations above (van de Hulst 1974) were developed for situations where the diffraction component is included in the particle albedo; because this is not true for Hapke's w_g, some restraint must be exercised in allowing g to approach 1, because such large values are generally only seen for phase functions that include diffraction.

(g1) One simple prediction for A_{so} is based on equation 10.23 or 10.51b of Hapke (1993; they are the same). These equations for the spherical albedo of a smooth, regolith-covered particle derive from the reflectivity of a semi-infinite layer of isotropic scatterers, and can be written in two slightly different ways:

$$A_{so} = \frac{1 - \gamma}{1 + \gamma} \left(1 - \frac{\gamma}{3(1 + \gamma)} \right) = r_o \left(1 - \frac{1 - r_o}{6} \right). \tag{25}$$

---

[7]A more recent model (Hapke 2002) has a more complete treatment of grain scattering asymmetry. The reader is invited to explore this approach as a possible refinement.

(g2) Cuzzi and Estrada (1998) used a slightly different, semi-empirical similarity technique from van de Hulst (1974, 1980):

$$A_{so} = \frac{(1 - \gamma_i)(1 - 0.139\gamma_i)}{1 + 1.17\gamma_i},\qquad(26)$$

using equation (24) for γ_i. We have compared the smooth particle spherical albedos from equations (25) and (26), and they agree to better than 1%, not surprising from comparison of their respective definitions.

(g3) A third approach combines models for smooth particle geometric albedo p (Hapke 1993, equation 10.38) and smooth particle phase function $\Phi(\alpha, w_g, 0) \equiv \Phi_o(\alpha)$ (Hapke 1993, equation 10.47), using the standard relation $A_{so} = pq$ (Hapke 1993, equation 10.54) with q given by equation (17) above and $P(\alpha)/P(0) = \Phi_o(\alpha)$. The smooth particle phase function $\Phi_o(\alpha)$ combines albedo-weighted Lambert and Lommel-Seeliger phase functions to represent the underlying multiple scattering component, with an explicit single-scattering term which is g-dependent. The opposition effect is neglected ($B = 0$), because it contributes negligibly to q, but the regolith grain phase function $P_g(\alpha)$ described above in 3f enters explicitly. Then,

$$p = r_o\left(\frac{1}{2} + \frac{1}{6}r_o\right) + \frac{w_g}{8}(P_g(0) - 1)\qquad(27)$$

and

$$\begin{aligned}
\Phi_o(\alpha) &= \frac{r_o}{2p}\left[\frac{(1 + \gamma)^2(P_g(\alpha) - 1)}{4} + (1 - r_o)\right]\left[1 - \sin\frac{\alpha}{2}\tan\frac{\alpha}{2}\mathrm{lncot}\frac{\alpha}{4}\right] \\
&+ \frac{4r_o^2}{6p}\left[\frac{\sin\alpha + (\pi - \alpha)\cos\alpha}{\pi}\right].
\end{aligned}\qquad(28)$$

Equation 27 involves approximations in the first term, and equation 28 is somewhat *ad hoc* (but plausible; see table 1 and section 1.4).

The optimum way to adapt this approach to anisotropic regolith grain scattering is unclear, and we have explored three approaches. Probably the most widely used approach (g3a) **uses the full Henyey-Greenstein regolith grain anisotropic phase function $P_g(\alpha)$, for arbitrary asymmetry factor** g, in the first order term $(1 + \gamma)^2(P_g(\alpha) - 1)/4$ above, and makes no further similarity adjustment (equation 23) to w_g. $\Phi_o(\alpha)$ must be renormalized for each choice of asymmetry parameter g; see section 2. As it turns out, this approach leads to results similar to (g1) and (g2) above in the range of (g, w_g) of most interest to icy bodies. Two other arguable approaches are to *make* the similarity correction to w_g, and either (g3b) continue to use the anisotropic single order scattering term as above, or (g3c) assume isotropic scattering ($g = 0$) in the first order term as well. Relative to the nominal case (g3a), option (g3b) leads to a stronger dependence of A_{so} on w_g, and option (g3c) leads to a weaker dependence.

The values of A_{so} predicted by (g1), (g2), and (g3a-c) are shown in figure 10 for the full range of w_g and g. For moderately high w_g and moderately positive g, they are not greatly different (and as noted above, g1 and g2 are nearly identical). The *overall* similarity of case g3c to cases (g1,g2) is misleading because what really matters to modeling observed spectra is the behavior in the appropriate *region* of (g, w_g) space. For the purpose of this paper we merely note that inferences as to the underlying composition of the material making up the regolith grains must be regarded as having a model-based uncertainty due to differences between these approaches at the tens of percent level in
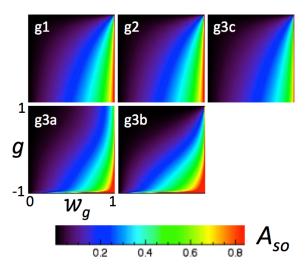
Figure 10: Five different approaches to calculating A_{so} as a function of regolith grain albedo $w_g = (0,1)$ and asymmetry parameter $g = (-1,1)$, as labeled on the lower left hand plot; see section 3 for definitions of the approaches denoted g1,2,3a,3b, and 3c. The effect of the anisotropic regolith grain phase function appearing explicitly in the first order term (g3a, g3b) is evident in the stronger dependence of A_{so} on g for those cases, especially at low w_g.

A_{so} over the range (g1,2)-(g3a,b,c). Poulet *et al.* (2003) also showed that different assumptions regarding the fine-scale distribution of compositional mixtures ("intimate" *vs.* "intramixed") can have significant quantitative implications about the average w_g and thus relative abundances.

(h) Following this "cookbook", one can trace the path connecting observed brightness spectra to the underlying composition. Inspection of the equations defining w_g (step d, above) shows that the regolith grain diameter D and the mass fraction f of intrinsic absorbing material enter only as their product fD. An application of this approach to determine particle composition from spectra of Saturn's rings can be found in Cuzzi *et al.* (2016).

4 Summary

Corrections to *spherical albedo* (also known as single-scattering albedo) of an isolated particle due to roughness and shadowing effects are not negligible, based on known phase functions. For an object such as Callisto (or Saturn's ring particles which have comparable phase functions), where $\mathcal{S} \sim 0.8$, the albedo correction due to rough surface scattering alone is almost 50%, and the albedo for Saturn's ring particles, for example, *without* roughness correction, has been estimated at around the same value (Dones *et al.* 1993, Doyle *et al.* 1989)! There are clearly implications for how much "absorber" one can add into the mixture *after* allowing for roughness, which in turn have important implications for the composition of surfaces of various objects. We see the most immediate application of these results as to objects that are studied photometrically over a range of phase angles, such as ring particles or near-Earth objects (NEOs).

In this paper we present a very simple way of treating roughness and shadowing effects that is based only on actual observations of some object's phase function. Practical use of the approach is outlined in section 3. The results are in decent general agreement with the more complicated forward model of Hapke (1993), and contain no explicit dependence on the albedo of the underlying surface. The exact functional form of the underlying surface facet shadowing function $f(\alpha)$ makes a little

difference (see figures 3 and 5) but once it has been determined (from observations *of* the phase function), it can be directly applied as a correction function for spherical albedo A_s; uncertainties *in* the shadowing function are probably smaller than errors induced by neglecting to apply *any* shadowing correction.

Acknowledgements

References

Akimov, L. A. 1980. On the nature of the opposition effect. *Vestnik Khar'kov Universitet* **204**, 3–12.

Bradley, E. T., J. E. Colwell, and L. W. Esposito 2013. Scattering properties of Saturn's rings in the far ultraviolet from Cassini UVIS spectra. *Icarus* **225**, 726–739.

Bradley, E. T., J. E. Colwell, L. W. Esposito, J. N. Cuzzi, H. Tollerud, and L. Chambers 2010. Far ultraviolet spectral properties of Saturn's rings from Cassini UVIS. *Icarus* **206**, 458–466.

Chandrasekhar, S. 1960. *Radiative Transfer*. Dover Publications, New York.

Ciarniello, M., F. Capaccioni, G. Filacchione, R. N. Clark, D. P. Cruikshank, P. Cerroni, A. Coradini, R. H. Brown, B. J. Buratti, F. Tosi, and K. Stephan 2011. Hapke modeling of Rhea surface properties through Cassini-VIMS spectra. *Icarus* **214**, 541–555.

Ciarniello, M. e. a. 2015. Cassini-VIMS observations of Saturn's main rings: II. A spectrophotometric study by means of Monte Carlo ray-tracing and Hapke's theory (in preparation). *Icarus* **999**.

Clark, R. N., D. P. Cruikshank, R. Jaumann, R. H. Brown, K. Stephan, C. M. Dalle Ore, K. Eric Livo, N. Pearson, J. M. Curchin, T. M. Hoefen, B. J. Buratti, G. Filacchione, K. H. Baines, and P. D. Nicholson 2012. The surface composition of Iapetus: Mapping results from Cassini VIMS. *Icarus* **218**, 831–860.

Cooke, M. L. 1991. *Saturn's rings: Photometric studies of the C Ring and radial variation in the Keeler Gap*. Ph. D. thesis, AA(Cornell Univ., Ithaca, NY.).

Cooke, M. L., P. D. Nicholson, and M. R. Showalter 1991. Photometric Studies of Saturn's C-Ring. In *Bulletin of the American Astronomical Society*, Volume 23 of *Bulletin of the American Astronomical Society*, pp. 1180.

Cord, A. M., P. C. Pinet, Y. Daydou, and S. D. Chevrel 2003. Planetary regolith surface analogs:. optimized determination of Hapke parameters using multi-angular spectro-imaging laboratory data. *Icarus* **165**, 414–427.

Cord, A. M., P. C. Pinet, Y. Daydou, and S. D. Chevrel 2005. Experimental determination of the surface photometric contribution in the spectral reflectance deconvolution processes for a simulated martian crater-like regolithic target. *Icarus* **175**, 78–91.

Cruikshank, D. P., T. C. Owen, C. Dalle Ore, T. R. Geballe, T. L. Roush, C. de Bergh, S. A. Sandford, F. Poulet, G. K. Benedix, and J. P. Emery 2005. A spectroscopic study of the surfaces of Saturn's large satellites: H_2O ice, tholins, and minor constituents. *Icarus* **175**, 268–283.

Cuzzi, J., R. Clark, G. Filacchione, R. French, R. Johnson, E. Marouf, and L. Spilker 2009. *Ring Particle Composition and Size Distribution*, pp. 459.

Cuzzi, J. N. 1985. Rings of Uranus - Not so thick, not so black. *Icarus* **63**, 312–316.

Cuzzi, J. N., J. E. Colwell, L. W. Esposito, C. C. Porco, C. D. Murray, P. D. Nicholson, L. J. Spilker, E. A. Marouf, R. C. French, N. Rappaport, and D. Muhleman 2002. Saturn's Rings: pre-Cassini Status and Mission Goals. *Space Science Reviews* **104**, 209–251.

Cuzzi, J. N., and P. R. Estrada 1998. Compositional Evolution of Saturn's Rings Due to Meteoroid Bombardment. *Icarus* **132**, 1–35.

Cuzzi, J. N., P. R. Estrada, and S. S. Davis 2014. Utilitarian Opacity Model for Aggregate Particles in Protoplanetary Nebulae and Exoplanet Atmospheres. *Astrophys. J. Supp.* **210**, 21.

Cuzzi, J. N., R. C. French, A. R. Hendrix, D. Olson, T. Roush, and S. Vahidinia 2016. . *Icarus, in preparation* **00**, 000–000.

Déau, E. 2015. The opposition effect in Saturn's main rings as seen by Cassini ISS: 2. Constraints on the ring particles and their regolith with analytical radiative transfer models. *Icarus* **253**, 311–345.

Déau, E., L. Dones, S. Charnoz, R. A. West, A. Brahic, J. Decriem, and C. C. Porco 2013. The opposition effect in Saturn's main rings as seen by Cassini ISS: 1. Morphology of phase functions and dependence on the local optical depth. *Icarus* **226**, 591–603.

Domingue, D. L., B. W. Denevi, S. L. Murchie, and C. D. Hash 2016. Application of multiple photometric models to disk-resolved measurements of Mercury's surface: Insights into Mercury's regolith characteristics. *Icarus* **268**, 172–203.

Dones, L., J. N. Cuzzi, and M. R. Showalter 1993. Voyager Photometry of Saturn's A Ring. *Icarus* **105**, 184–215.

Doyle, L. R., L. Dones, and J. N. Cuzzi 1989. Radiative transfer modeling of Saturn's outer B ring. *Icarus* **80**, 104–135.

Elliott, J. P., and L. W. Esposito 2011. Regolith depth growth on an icy body orbiting Saturn and evolution of bidirectional reflectance due to surface composition changes. *Icarus* **212**, 268–274.

Emery, J. P., and R. H. Brown 2004. The surface composition of Trojan asteroids: constraints set by scattering theory. *Icarus* **170**, 131–152.

Filacchione, G., F. Capaccioni, R. N. Clark, P. D. Nicholson, D. P. Cruikshank, J. N. Cuzzi, J. I. Lunine, R. H. Brown, P. Cerroni, F. Tosi, M. Ciarniello, B. J. Buratti, M. M. Hedman, and E. Flamini 2013. The Radial Distribution of Water Ice and Chromophores across Saturn's System. *ApJ* **766**, 76.

French, R. G., A. Verbiscer, H. Salo, C. McGhee, and L. Dones 2007. Saturn's Rings at True Opposition. *PASP* **119**, 623–642.

Goguen, J. D., T. C. Stone, H. H. Kieffer, and B. J. Buratti 2010. A new look at photometry of the Moon. *Icarus* **208**, 548–557.

Hapke, B. 1993. *Theory of reflectance and emittance spectroscopy*. Cambridge, UK: Cambridge University Press, —c1993.

Hapke, B. 2002. Bidirectional Reflectance Spectroscopy. 5. The Coherent Backscatter Opposition Effect and Anisotropic Scattering. *Icarus* **157**, 523–534.

Hapke, B. 2012. *Theory of reflectance and emittance spectroscopy, 2nd Edition*. Cambridge, UK: Cambridge University Press, —c2012.

Hapke, B. 2013. Comment on "A critical assessment of the Hapke photometric model" by Y. Shkuratov et al. *J. Quant. Spect. Rad. Transf.* **116**, 184–190.

Harris, D. L. 1961. *Photometry and Colorimetry of Planets and Satellites*, pp. 272.

Hedman, M. M., P. D. Nicholson, J. N. Cuzzi, R. N. Clark, G. Filacchione, F. Capaccioni, and M. Ciarniello 2013. Connections between spectra and structure in Saturn's main rings based on Cassini VIMS data. *Icarus* **223**, 105–130.

Helfenstein, P., and M. K. Shepard 2011. Testing the Hapke photometric model: Improved inversion and the porosity correction. *Icarus* **215**, 83–100.

Hendrix, A. R., and C. J. Hansen 2008. Ultraviolet observations of Phoebe from the Cassini UVIS. *Icarus* **193**, 323–333.

Jehl, A., P. Pinet, D. Baratoux, Y. Daydou, S. Chevrel, F. Heuripeau, N. Manaud, A. Cord, C. Rosemberg, G. Neukum, K. Gwinner, F. Scholten, H. Hoffman, T. Roatsch, and the HRSC Team 2008. Gusev photometric variability as seen from orbit by HRSC/Mars-express. *Icarus* **197**, 403–428.

Kreslavsky, M. A., Y. G. Shkuratov, Y. I. Velikodsky, V. G. Kaydash, D. G. Stankevich, and C. M. Pieters 2000. Photometric properties of the lunar surface derived from Clementine observations. *JGR* **105**, 20281–20296.

Liou, K. N., Q. Cai, J. B. Pollack, and J. N. Cuzzi 1983. Light scattering by randomly oriented cubes and parallelepipeds. *App. Optics* **22**, 3001–3008.

Liou, K.-N., and J. E. Hansen 1971. Intensity and Polarization for Single Scattering by Polydisperse Spheres: A Comparison of Ray Optics and Mie Theory. *Journal of Atmospheric Sciences* **28**, 995–1004.

Lumme, K., and E. Bowell 1981a. Radiative transfer in the surfaces of atmosphereless bodies. I - Theory. *Astron. J.* **86**, 1694–1704.

Lumme, K., and E. Bowell 1981b. Radiative transfer in the surfaces of atmosphereless bodies. II. Interpretation of Phase Curves. *Astron. J.* **86**, 1705–1721.

Minnaert, M. 1961. *Photometry of the Moon*. Univ of Chicago.

Muinonen, K., H. Parviainen, J. Näränen, J.-L. Josset, S. Beauvivre, P. Pinet, S. Chevrel, D. Koschny, B. Grieger, and B. A. S.-. Foing 2011. Lunar mare single-scattering, porosity, and surface-roughness properties with SMART-1 AMIE. *Astron. Astrophys.* **531**, A150.

Mushkin, A., and A. R. Gillespie 2006. Mapping sub-pixel surface roughness on Mars using high-resolution satellite image data. *Geophys. Res. Lett.* **33**, L18204.

Penttilä, A., V. G. Shevchenko, O. Wilkman, and K. Muinonen 2016. H, G_1, G_2 photometric phase function extended to low-accuracy data. *Planet. Sp. Sci.* **123**, 117–125.

Pilorget, C., J. Fernando, B. L. Ehlmann, F. Schmidt, and T. Hiroi 2016. Wavelength dependence of scattering properties in the VIS-NIR and links with grain-scale physical and compositional properties. *Icarus* **267**, 296–314.

Pitman, K. M., B. J. Buratti, and J. A. Mosher 2010. Disk-integrated bolometric Bond albedos and rotational light curves of saturnian satellites from Cassini Visual and Infrared Mapping Spectrometer. *Icarus* **206**, 537–560.

Porco, C. C., J. W. Weiss, D. C. Richardson, L. Dones, T. Quinn, and H. Throop 2008. Simulations of the Dynamical and Light-Scattering Behavior of Saturn's Rings and the Derivation of Ring Particle and Disk Properties. *Astronomical Journal* **136**, 2172–2200.

Poulet, F., D. P. Cruikshank, J. N. Cuzzi, T. L. Roush, and R. G. French 2003. Compositions of Saturn's rings A, B, and C from high resolution near-infrared spectroscopic observations. *Astron. Astrophys.* **412**, 305–316.

Poulet, F., and J. N. Cuzzi 2002. The Composition of Saturn's Rings. *Icarus* **160**, 350–358.

Poulet, F., J. N. Cuzzi, D. P. Cruikshank, T. Roush, and C. M. Dalle Ore 2002. Comparison between the Shkuratov and Hapke Scattering Theories for Solid Planetary Surfaces: Application to the Surface Composition of Two Centaurs. *Icarus* **160**, 313–324.

Roush, T. L. 1994. Charon: More than water ice? *Icarus* **108**, 243–254.

Salo, H., and R. G. French 2010. The opposition and tilt effects of Saturn's rings from HST observations. *Icarus* **210**, 785–816.

Salo, H., and R. Karjalainen 2003. Photometric modeling of Saturn's ringsI. Monte Carlo method and the effect of nonzero volume filling factor. *Icarus* **164**, 428–460.

Shepard, M. K., and P. Helfenstein 2011. A laboratory study of the bidirectional reflectance from particulate samples. *Icarus* **215**, 526–533.

Shevchenko, V. G., I. N. Belskaya, K. Muinonen, A. Penttilä, Y. N. Krugly, F. P. Velichko, V. G. Chiorny, I. G. Slyusarev, N. M. Gaftonyuk, and I. A. Tereschenko 2016. Asteroid observations at low phase angles. IV. Average parameters for the new H, G_1, G_2 magnitude system. *Planet. Sp. Sci.* **123**, 101–116.

Shkuratov, Y., V. Kaydash, V. Korokhin, Y. Velikodsky, D. Petrov, E. Zubko, D. Stankevich, and G. Videen 2012. A critical assessment of the Hapke photometric model. *J. Quant. Spect. Rad. Transf.* **113**, 2431–2456.

Shkuratov, Y., V. Kaydash, V. Korokhin, Y. Velikodsky, D. Petrov, E. Zubko, D. Stankevich, and G. Videen 2013. Response to the comment by B. Hapke on "A critical assessment of the Hapke photometric model". *J. Quant. Spect. Rad. Transf.* **116**, 191–195.

Shkuratov, Y., L. Starukhina, H. Hoffmann, and G. Arnold 1999. A Model of Spectral Albedo of Particulate Surfaces: Implications for Optical Properties of the Moon. *Icarus* **137**, 235–246.

Shkuratov, Y. G., M. A. Kreslavsky, A. A. Ovcharenko, D. G. Stankevich, E. S. Zubko, C. Pieters, and G. Arnold 1999. Opposition Effect from Clementine Data and Mechanisms of Backscatter. *Icarus* **141**, 132–155.

Shkuratov, Y. G., D. G. Stankevich, D. V. Petrov, P. C. Pinet, A. M. Cord, Y. H. Daydou, and S. D. Chevrel 2005. Interpreting photometry of regolith-like surfaces with different topographies: shadowing and multiple scattering. *Icarus* **173**, 3–15.

Souchon, A. L., P. C. Pinet, S. D. Chevrel, Y. H. Daydou, D. Baratoux, K. Kurita, M. K. Shepard, and P. Helfenstein 2011. An experimental study of Hapke's modeling of natural granular surface samples. *Icarus* **215**, 313–331.

Squyres, S. W., and J. Veverka 1981. Voyager photometry of surface features on Ganymede and Callisto. *Icarus* **46**, 137–155.

Stedman, R. W. 1977. *Serials: Suspense and Drama By Installment*. University of Oklahoma Press.

van de Hulst, H. C. 1957. *Light Scattering by Small Particles*.

van de Hulst, H. C. 1974. The spherical albedo of a planet covered with a homogeneous cloud layer. *Astron. Astrophys.* **35**, 209–214.

van de Hulst, H. C. 1980. *Multiple light scattering. Vols._1_and_2*.

Verbiscer, A. J., P. Helfenstein, and B. J. Buratti 2013. *Photometric Properties of Solar System Ices*, pp. 47.

Veverka, J., P. Helfenstein, A. Skypeck, and P. Thomas 1989. Minnaert photometric parameters for the satellites of Uranus. *Icarus* **78**, 14–26.